Bulletin of the Seismological Society of America, Vol. 99, No. 6, pp. 3314–3325, December 2009, doi: 10.1785/0120090061

A Simultaneous Multiphase Approach to Determine *P*-Wave and *S*-Wave Attenuation of the Crust and Upper Mantle

by Michael E. Pasyanos, William R. Walter, and Eric M. Matzel

Abstract We have generalized the methodology of our regional amplitude tomography from the *Lg* phase to the four primary regional phases (*Pn*, *Pg*, *Sn*, *Lg*). Differences in the geometrical spreading, source term, site term, and travel paths are accounted for, while event source parameters such as seismic moment are consistent among phases. In the process, we have developed the first comprehensive regional *P*-wave and *S*-wave attenuation model of the crust and upper mantle by simultaneously using the amplitudes of four regional phases. When applied to an area encompassing the Middle East, eastern Europe, western Asia, south Asia, and northeast Africa for the 1–2 Hz passband, we find large differences in the attenuation of the lithosphere across the region. The tectonic Tethys collision zone has high attenuation, while stable outlying regions have low attenuation. While crust and mantle Q variations are often consistent, we do find several notable areas where they differ considerably but are appropriate given the region's tectonic history. Lastly, the relative values of Qp and Qs indicate that scattering Q is likely the dominant source of attenuation in the crust at these frequencies.

Introduction

In a previous study, Pasyanos *et al.* (2009), which this article builds on, we modified the standard regional attenuation tomography technique (e.g., Sereno *et al.*, 1988) to more explicitly define the source expression in terms of an earthquake source model with the seismic moment M_o. We then used thousands of *Lg* amplitudes in the Middle East to model *S*-wave crustal attenuation in the frequency band from 0.5 to 10 Hz. We found large variations in the attenuation parameter Q, which corresponded well to tectonic processes of the region, most notably the tectonic age. We also found that the power-law model of frequency-dependent attenuation might not be the most appropriate parameterization across this frequency band for all regions that we studied.

In this article we model the apparent amplitude attenuation of the four main regional phases: *Pn*, *Pg*, *Sn*, and *Lg*. We consider these phases in their broadest definitions: where *Pg* and *Lg* represent *P*- and *S*-wave energy traveling in the crust, and *Pn* and *Sn* represent energy traveling in the uppermost mantle lid. In this sense *Pg* and *Lg* include both direct rays and crustal reverberations (e.g., *PmP* and *SmS* and their multiples). We treat *Pn* and *Sn* as turning rays in the mantle lid rather than true head waves based on the observed character of signals. The *Pn* and *Sn* signals often have similar frequency content to the crustal phases rather than the integrated source spectrum expected for true head waves. In this sense *Pn* and *Sn* represent energy traveling in the lid as a whispering gallery phase or as a multiply reflected turning ray.

We develop the methodology for the multiple regional phase attenuation problem in a similar manner as our previous study for a single phase, by formulating the amplitudes of the four regional phases in terms of a common source moment with differences between phases in the geometrical spreading, path attenuation, and site effects. This is very similar to the formulation presented by Walter and Taylor (2001). This methodology allows us to then use the amplitudes of all four phases simultaneously to determine the *P*- and *S*-wave attenuation of the crust and upper mantle. Here we limit the scope relative to the previous study by looking at only amplitudes in a single frequency band (1–2 Hz), but the same analysis could readily be extended to other frequency bands or a suite of frequency bands.

A number of previous studies of attenuation in the region have used a variety of methods, including the relative amplitudes of direct phases (e.g., Sandvol *et al.*, 2001; Al–Damegh *et al.*, 2004); two station methods (Zor *et al.*, 2007); *Lg* coda (Mitchell *et al.*, 1997); propagation efficiency and blockage (Mellors *et al.*, 1999; Gok *et al.*, 2000; McNamara and Walter, 2001; Gok *et al.*, 2003); and surface waves (Levshin *et al.*, 2008). These studies, however, tended to focus on the attenuation or efficiency of each phase separately. When inversions for the attenuation of seismic phases are performed separately, inconsistencies can be introduced. For example, the attenuation for the crustal legs of *Pn* might be incompatible with the crustal attenuation of *Pg* amplitudes in the same region.

Additionally, source term parameters, such as M_o and apparent stress, can be different among the phases for the same events that would be nonphysical.

We will first present the methodology by reviewing our previous work and denoting where the technique used here differs. We next examine the new dataset of regional phases, amplitude measurements, and the four-phase tomography method. We then discuss our results, focusing on how crust and upper mantle attenuation relate to the tectonic framework of our study area. We will critically compare the crust and upper mantle attenuation, as well as the relative attenuation of P waves and S waves. Finally, we will also examine and interpret the source and site terms.

Methodology

The amplitude of seismic phases is controlled by the source excitation, S; geometrical spreading, G; attenuation, B; and site effects, P. For a given frequency, this is usually represented by the expression

$$A_{ij} = S_i G_{ij} B_{ij} P_j, \quad (1)$$

where i is the event index and j is the station index. In Pasyanos *et al.* (2009), we used this parameterization for Lg amplitudes and defined the earthquake source in terms of M_o. Here, we will extend the technique to phases Pn, Pg, and Sn by defining how each of these terms differs from Lg and from each other for the other phases. By using both mantle and crustal phases, we can better isolate the distribution of attenuation in the lithosphere. By also using a variety of phases, we can ensure that moment terms are consistent among the phases, as long as we invert all of the amplitude information simultaneously. We consider each of the terms of equation (1) in turn.

Geometrical Spreading Term

The geometrical spreading term G_{ij} is represented by a critical distance variable, R_o, and a spreading variable, n (Street *et al.*, 1975). While the parameters for Lg are generally agreed upon (e.g., Street *et al.*, 1975; Chavez and Priestley, 1986; Yang, 2002), and the parameters for the crustal phases Pg and Lg are expected to be somewhat similar (McCormack *et al.*, 1994; Walter and Taylor, 2001), they differ significantly for the upper mantle phases Pn and Sn. The critical distance, R_o, is set low (1 km) for phases Pn and Sn. Setting the geometrical spreading term correctly is important because both the attenuation term and the geometrical spreading term depend on distance and can trade off with each other. A higher value for the geometrical spreading parameter, n, results in less anelastic attenuation and, hence, higher Q. If the geometrical spreading is too high, it can result in negative values of Q, which are nonphysical, as it would increase amplitudes from attenuation alone with distance. Unfortunately, resolving between the geometrical spreading and attenuation terms is often somewhat difficult. Sereno *et al.* (1988) suggest a value of 1.3 for the geometrical spreading of Pn, while the magnitude and distance amplitude correction (MDAC) formulation (Walter and Taylor, 2001) suggests that 1.1 might be a more appropriate value. Taylor *et al.* (2002) conducted a grid search of parameters and found that 1.3 works best for Pn and 1.1 for Sn in western China. While the absolute values of Q change with variations in n, the relative variation in Q does not, nor does the overall fit to the amplitudes.

A recent article by Yang *et al.* (2007) considered a more general geometrical spreading for Pn and Sn that differed from the spreading of a classical head wave and was frequency-dependent. These same authors, however, found that this broke down to a more traditional geometrical spreading as scatterers were introduced. We use a value of 1.1 for both Pn and Sn, which minimizes the occurrence of nonphysical infinite or negative Qs, and remind the reader that the absolute value of Q in the mantle is influenced strongly by the choice of geometrical spreading. Table 1 shows the values of the geometrical spreading terms for each phase.

Source Term

As in our previous study, we used the MDAC formulation (Walter and Taylor, 2001) to tie the source term, S_i, to seismic moment, M_o. While the moments are the same for each phase, the P-wave source term S^P differs from the S-wave source term S^S through the radiated energy related term F and potentially differing corner frequencies ω_c

$$S^P = F^P M_o / [1 + (\omega/\omega_c^P)^2] \quad (2)$$

$$S^S = F^S M_o / [1 + (\omega/\omega_c^S)^2]. \quad (3)$$

For convenience, we have set the P-wave and S-wave corner frequencies (as defined in Pasyanos *et al.*, 2009) to be the same: $\omega_c^P = \zeta\omega_c^S (\zeta = 1)$, which fixes the ratio between the P-wave source term, S^P, and S-wave source term, S^S, but making the two different $(\zeta \neq 1)$ simply makes the source term a function of the corner-frequency or moment. Tests indicate that as ζ increases (and the P-wave corner increases relative to the S-wave corner), Qp will decrease slightly relative to Qs (which does not change), but not otherwise affect the distribution of anomalies. With the corner frequencies the same, the ratio of the P-wave and S-wave source terms simply become the ratio of the F terms for P waves and S waves. As found by Zhang *et al.* (2002), at the high frequencies that we

Table 1
Geometrical Spreading Term Parameters Used for Each Phase

Phase	n	R_o (km)
Pg, Lg	0.5	100
Pn, Sn	1.1	1

are considering here, there is a lot of scattering for all phases and the amplitude effect due to the radiation pattern is not predictable. Instead, we use the average *P*-wave and *S*-wave radiation patterns.

The *F* terms for *P*-wave phases (*Pn*, *Pg*) and *S*-wave phases (*Sn*, *Lg*) are, respectively

$$F^P = R^P_{\theta\phi}/4\pi\sqrt{\rho_s\rho_r\alpha_s^5\alpha_r} \quad (4)$$

$$F^S = R^S_{\theta\phi}/4\pi\sqrt{\rho_s\rho_r\beta_s^5\beta_r}. \quad (5)$$

We use the following values for terms in these equations:

average *P*-wave radiation pattern: $R^p_{\theta\phi} = 0.44$ (from Boore and Boatwright, 1984)
average *S*-wave radiation pattern: $R^S_{\theta\phi} = 0.60$ (from Boore and Boatwright, 1984)
source density: $\rho_s = 2700\ \mathrm{kg/m^3}$
receiver density: $\rho_r = 2500\ \mathrm{kg/m^3}$
source *S*-wave velocity: $\beta_s = 3500\ \mathrm{m/sec}$
receiver *S*-wave velocity: $\beta_r = 2900\ \mathrm{m/sec}$
source *P*-wave velocity: $\alpha_s = 6000\ \mathrm{m/sec}$
receiver *P*-wave velocity: $\alpha_r = 5000\ \mathrm{m/sec}$

Plugging these values into equations (4) and (5), we find $F^P = 6.83\mathrm{e}{-17}$ and $F^S = 4.71\mathrm{e}{-16}$; hence, $F^S = 6.89F^P$ and $S^S = 6.89S^P$. We will make use of this relationship in the inversion because we only want to solve for one value of the M_o parameter for each event.

Site Term

The site term, P_j, which represents the amplification due to local structure at the station, is similar to the definition in Pasyanos *et al.* (2009). The only major difference is that there should be at least two site terms for each station: a *P*-wave term and an *S*-wave term. We have considered the question of whether four terms are needed: one for each phase. Because the site term is local near-station effect, however, we have assumed that the site terms for *Pn* and *Pg* are the same, as are the site terms for *Sn* and *Lg*; therefore, we use only two site terms, one for *P* and one for *S*.

Attenuation Term

Obviously, the regional phases *Pn*, *Pg*, *Sn*, and *Lg* each traverse different paths through the crust, and, in case of some phases, the upper mantle. They are, in fact, what define the phases (e.g., Storchak *et al.*, 2003); the term has to reflect the differing paths. The attenuation term can be generalized as

$$B_{ij} = \exp\left[-\frac{\omega}{2}\sum_{k=1}^{n\mathrm{layers}}\frac{r_k}{Q_k v_k}\right], \quad (6)$$

where *r* is the distance in each layer, *Q* represents the attenuation parameters, v is the velocity, and *k* is the layer number.

We have simplified this task by parameterizing the crust and upper mantle as a two-layer (true layer over a half-space) model shown in Table 2. This makes the problem more straightforward by modeling the attenuation of *Pg* and *Lg* as attenuation of a straight ray path in the crustal layer and distributing the attenuation of *Pn* and *Sn* by a simple geometrical ray path through the crust and upper mantle.

For *Pg* and *Lg*, this becomes

$$B_{ij} = \exp[(-\omega r_c)/(2Q_c v_c)], \quad (7)$$

where r_c, Q_c, and v_c are the crustal distance, attenuation parameter, and velocity, respectively. For *Pn* and *Sn*, the term becomes

$$B_{ij} = \exp[(-\omega r_{c1})/(2Q_{c1}v_{c1}) + (-\omega r_m)/(2Q_m v_m) + (-\omega r_{c2})/(2Q_{c2}v_{c2})], \quad (8)$$

where r_m, Q_m, and v_m are the same parameters for the upper mantle; r_{c1}, r_{c2}, Q_{c1}, Q_{c2}, v_{c2}, and v_{c2} are the parameters for the crustal legs (at the source and station ends) of the phase.

This could be generalized to a many-layer model, although a ray tracer (or full-sensitivity kernel) would have to be employed to determine the specific phase path. Additional complications might arise if the phase is actually comprised of multiple rays, but in most cases the overall amplitude of the phase could be modeled by amplitude of the dominant ray path. Moreover, coverage of the region would have to be exceptional in order to resolve the attenuation among the crustal layers. For the moment, while recognizing the limitations, the two-layer model can capture a significant portion of the amplitude variation from attenuation.

Inversion

Similar to Pasyanos *et al.* (2009), we invert the amplitude data by taking the base-10 logarithm and correcting for the geometrical spreading term. In addition, because we are combining *P*-wave and *S*-wave amplitude information, we need to correct for the difference in the source terms. We can do this either by correcting the *P*-wave amplitudes (by adding log 6.89 or 0.838) and solving for the *S*-wave source terms, or by correcting the *S*-wave amplitudes (by subtracting 0.838)

Table 2
Velocity Model Used

Layer	Depth (km)	V_P (km/sec)	V_S (km/sec)
Crust	0–30	6.50	3.70
Upper mantle	30–	8.00	4.50

and solving for the *P*-wave source terms. The approaches are equivalent; either source term can then be solved for the appropriate M_o. Equation (1) becomes for *P*- and *S*-wave amplitude

$$A_{ij}^P = S_i^P G_{ij}^P B_{ij}^P P_j^P \tag{9}$$

and

$$A_{ij}^S = S_i^S G_{ij}^S B_{ij}^S P_j^S = 6.89 S_i^P G_{ij}^S B_{ij}^S P_j^S. \tag{10}$$

In log space, correcting for geometrical spreading and substituting the source terms and attenuation, for *P*-wave amplitudes we get

$$\log A_{ij}^P - \log G_{ij}^P = \log S_i^P + \log P_j^P - [(\omega \log e)/(2Q_{ij}^P v^P)]R_{ij}, \tag{11}$$

and for *S*-wave amplitudes we get

$$\log A_{ij}^S - \log G_{ij}^S = \log S_i^S + \log P_j^S - [(\omega \log e)/(2Q_{ij}^S v^S)]R_{ij}, \tag{12}$$

which, when substituting the *P*-wave source term, becomes

$$\log A_{ij}^S - \log G_{ij}^S - 0.838 = \log S_i^P + \log P_j^S - [(\omega \log e)/(2Q_{ij}^S v^S)]R_{ij}. \tag{13}$$

Through equations (11) and (13) we now have a system of equations we can use for the amplitudes of each regional phase that are all functions of Qp and Qs in the crust and upper mantle, the *P*-wave and *S*-wave site terms, and a single source term. We then proceed to use amplitude information from *Pn*, *Pg*, *Sn*, and *Lg* to solve for all attenuation parameters, site terms, and source terms simultaneously. The tradeoffs among the terms of equation (1) are discussed in Pasyanos *et al.* (2009).

Data and Tomography

We have started with the dataset from Pasyanos *et al.* (2009), measuring amplitudes of *Pn*, *Pg*, and *Sn*, in addition to *Lg*. We then expanded our study area in all directions, but farthest to the north into the Russian platform, and measured new events at existing stations. Finally, we added stations in the newly expanded region to the north in Russia (OBN, ARU, MHV, PUL), northeast in Kazakhstan and western China (BRVK, MAKZ, WUS, ZAL, KURK), northwest in eastern Europe (KIEV, FINES, MLR, VTS, KWP, SUW), and slightly to the south (PALK, FURI, AAE). We have also in-filled the Middle East by adding data from several temporary deployments, including some stations from the Mantle Investigation of the Deep Suture between Europe and Africa experiment and several Program for Array Seismic Studies of the Continental Lithosphere deployments in Ethiopia, eastern Turkey, and Pakistan. All in all, we have a total of 106 stations.

We use the same signal-to-noise ratio (SNR) criteria as that from Pasyanos *et al.* (2009): a preevent SNR of 2.0 and prephase SNR of 1.0. As in the previous study, every waveform is analyst reviewed. If identified, the phase arrival times are picked. Otherwise, theoretical arrival times are used. The theoretical phase velocities vary from region to region depending on the regional structure, but range from 7.9 to 8.3 km/sec for *Pn*, 5.85 to 6.3 km/sec for *Pg*, 4.5 to 4.65 km/sec for *Sn*, and 3.3 to 3.6 km/sec for *Lg*. Also, it is our general practice to make measurements from several available channels (e.g., BHZ, HHZ, SHZ) from a station in case any one is not available to record a particular event.

We start with a total of 11,721 event-station-channel combinations, which is nearly double the overall number (5889) we had in Pasyanos *et al.* (2009) at 1 Hz. Because we have a larger dataset than our previous study, we can afford to be choosier about our data. Therefore, we have eliminated any events that have only been recorded by a single station, in order to reduce any potential tradeoffs among terms. We also only use one channel for any given event—station path. After eliminating these, we have 10,020 unique event-station paths with picks (Fig. 1).

Of the four regional phases, we have the most paths for *Pn* (8178). We have fewer paths for *Sn* (6554), which, not being a first-arriving phase, generally has a lower SNR. *Sn* is also blocked in particular regions such as eastern Turkey

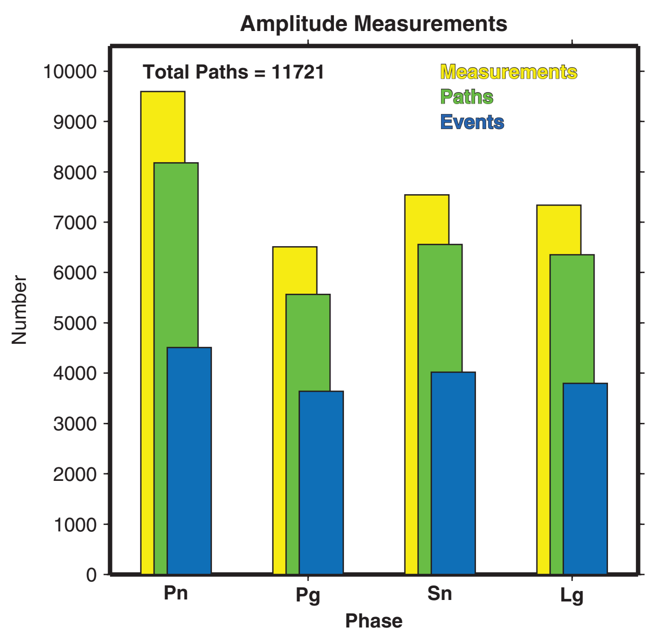

Figure 1. Number of *Pn*, *Pg*, *Sn*, and *Lg* measurements (yellow), paths (green), and events (blue) passing the signal-to-noise criteria. The measurements are recorded on 107 stations.

(Gök *et al.*, 2000). We also have fewer paths for *Lg* (6353), which can propagate to longer distances than *Pn* and *Sn*, but suffers from phase blockage in certain regions, notably oceanic regions and other regions where the crust thins (Zhang and Lay, 1995). Lastly, we have significantly fewer paths for *Pg* (5567), which does not propagate to longer distances as well as *Lg*.

In all cases, however, we have somewhat similar coverage of our study area (Fig. 2). All phases have excellent coverage of a wide swath encapsulating the Tethys Belt and extending down the Red Sea and Gulf of Aden to include Arabia. The Indian subcontinent is only sparsely covered to the northwest. We have significantly poorer coverage in Russia, northeast Africa, and the oceanic regions, where a lack of seismicity results in significantly fewer paths recording regional phases. Blanketing the study area with amplitude measurements is necessary in this region because of the large amplitude changes we see over short distances. For example, Figure 3 shows large changes in *Lg* amplitudes recorded at station MALT between a southern group that crosses the Arabian platform and a northern group in which propagation stays within the Turkish plateau. The northern group has much smaller *Lg* amplitudes than the southern group.

The next step in the inversion is to populate the initial values of Q, S, and P in the inversion. The source term, S_i, is set to the appropriate value for the moment and phase (equations 2 and 3). Moments are either taken from available catalogs, estimated from regional waveform modeling, or derived from coda waves, as explained in detail in Pasyanos *et al.* (2009). Where these options are not available, moments are estimated from other magnitudes. The site term, P_j, for both P waves and S waves is initialized to 1.0.

For starting values of Qs and Qp in the crust, we set terms S and P and inverted for the best 1D value using *Lg* only and *Pg* only, respectively. We then use these values in the crust and solve for the best values of Q in the mantle using *Sn* and *Pn*. We find a starting value of $Qp = 300$ and $Qs = 300$ for the crust and $Qp = 800$ and $Qs = 400$ for the upper mantle. We note that in the crust, these values differ significantly from the relationships often used to relate Qp and Qs [e.g., $Qp = (9/4)\ Qs$ (derived from Anderson and Hart, 1978, where $V_P/V_S = \sqrt{3}$); $Qp = 1.5\ Qs$ (Olsen *et al.*, 2003)]. This could, in part, be due to the fact that we are solving for apparent attenuation (which is a combination of intrinsic and scattering attenuation), and not simply intrinsic attenuation alone, where we might expect these relations to hold.

We have gridded our study area into 0.5° blocks. A Laplacian function smooths Q variation within the crust and upper mantle, but there is no additional constraint between the attenuation of the crust and upper mantle. A conjugate gradient solver is then used on the combined series of equations. We solve for a total of seven sets of parameters: (1) crustal Qs, (2) upper mantle Qs, (3) crustal Qp, (4) upper mantle Qp, (5) *S*-wave site terms, (6) *P*-wave site terms, and (7) source terms.

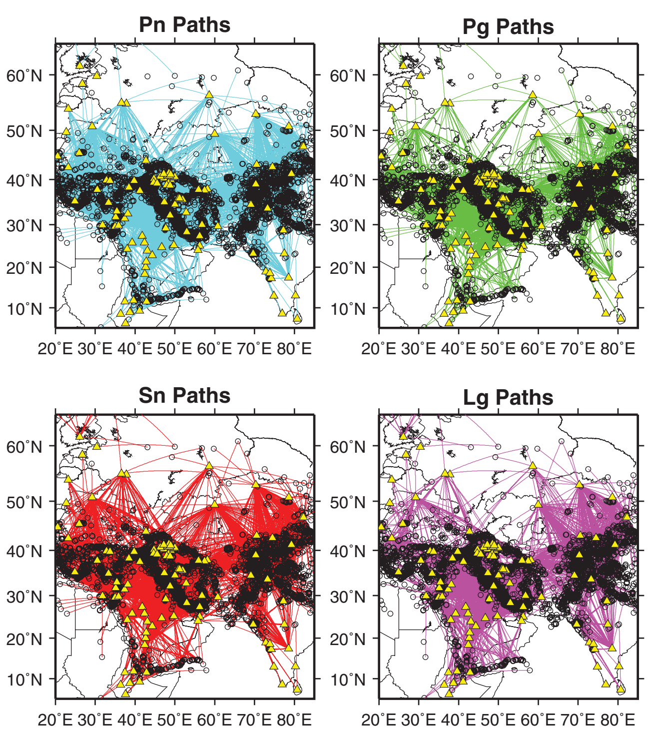

Figure 2. Path map of *Pn*, *Pg*, *Sn*, *Lg* attenuation measurements in our study area. Stations are shown as yellow triangles, events as black circles, and paths as cyan lines (*Pn*), green lines (*Pg*), red lines (*Sn*), and purple lines (*Lg*).

Results

In running the inversion, one of our first tests was in comparing crustal Qs determined from *Lg* phases only to the crustal Qs obtained using all phases. The results are almost identical. We performed similar tests for crustal Qp derived from *Pg* amplitude data (which also looked nearly identical), before running the full four-phase inversion. Checkerboard resolution tests reveal that we are able to completely recover the input pattern at 5° over the whole coverage region, while we are able to recover 3° and 2° patterns over a large portion of the study area encompassing Arabia, Turkey, Iran, and into eastern Kazakhstan. Further tests indicate that there is little bleeding of the input model from the crust into the mantle and vice versa.

When we run the full four-phase inversion on the actual dataset, the overall variance reduction is high. Initial misfit of the data is about 0.884 log-amplitude units, with slightly higher misfit (~1.1) for the *Lg* phase. After inversion, this misfit is reduced to 0.319 log-amplitude, and the misfit is approximately the same for all the phases. Results of the inversion for the attenuation parameter Q are shown in Figure 4. Panels show the following: (a) crustal Qs; (b) upper mantle Qs; (c) crustal Qp; and (d) upper mantle Qp. While it might be tempting to refer to the crustal Qs and Qp as Q_{Lg} and Q_{Pg} (and upper mantle Qs and Qp as Q_{Sn} and Q_{Pn}),

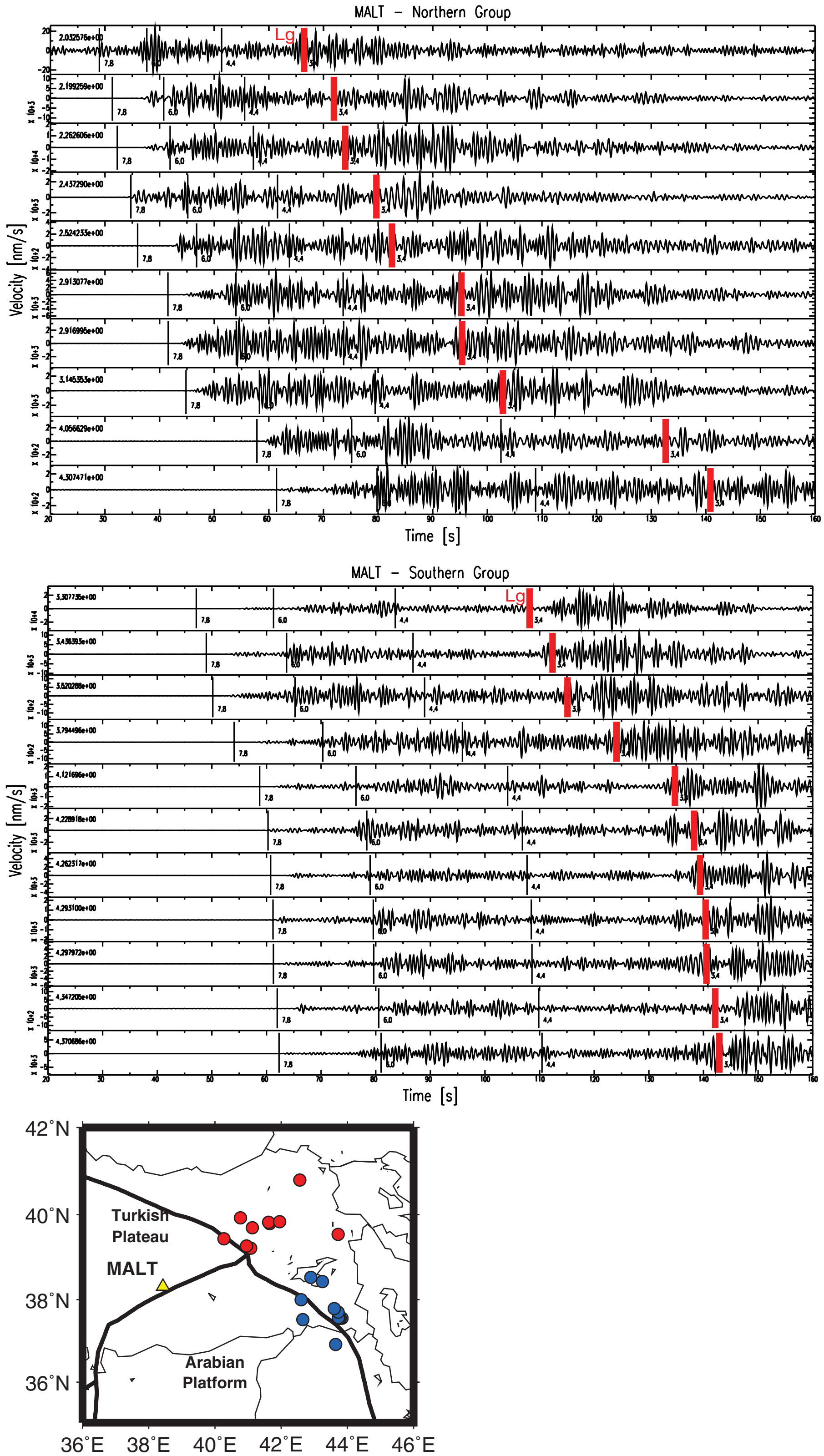

Figure 3. Waveforms for two sets of events recorded at station MALT (Malatya, Turkey): a northern group (which crosses the Turkish plateau) and a southern group (which crosses the Arabian platform). All traces have been filtered between 1.0 and 2.0 Hz. The approximate arrival of the *Lg* phase (3.4 km/sec) is highlighted in red. Inset shows the locations of the northern group (red circles), the southern group (blue circles), and the recording station (yellow triangle).

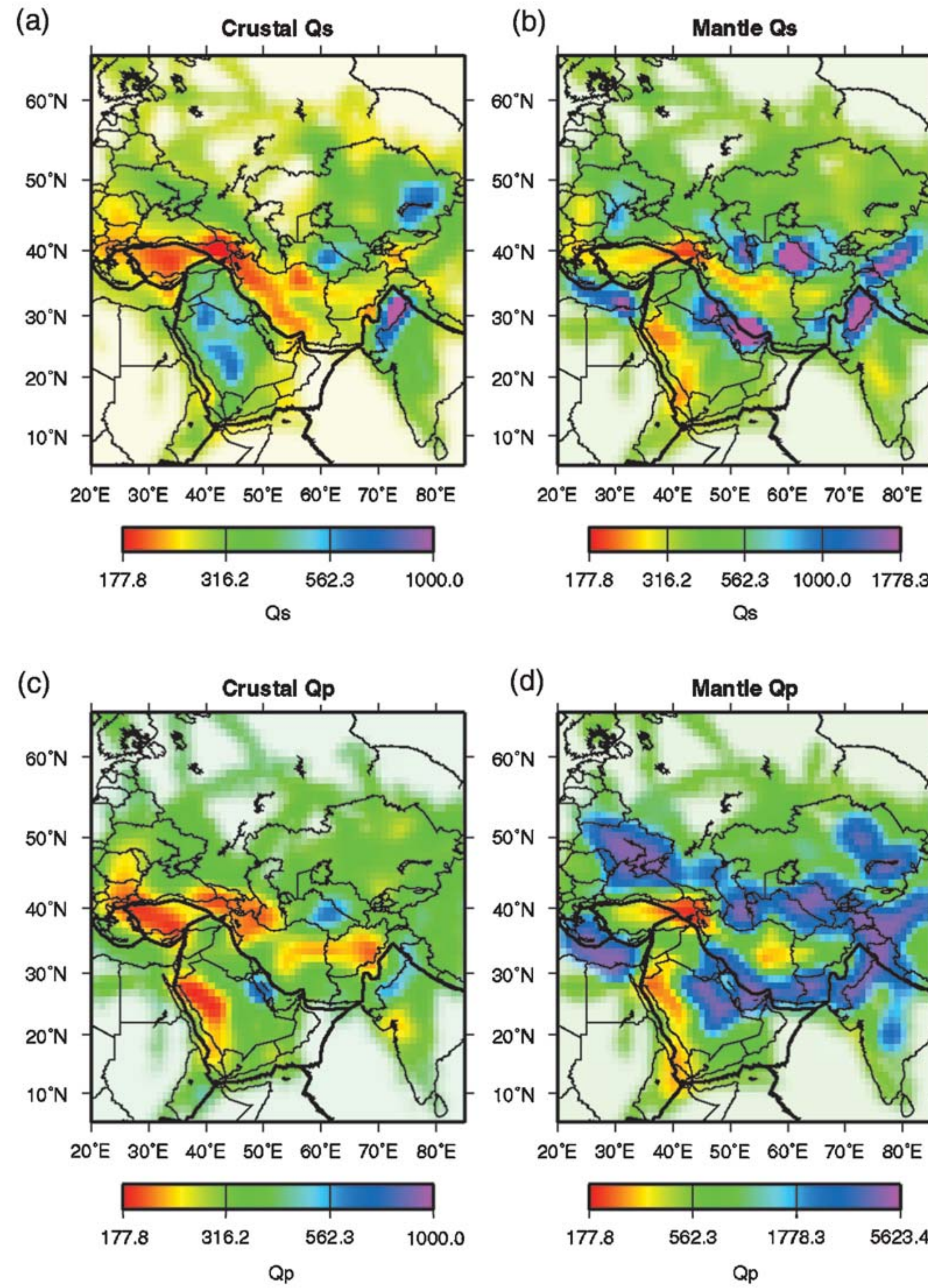

Figure 4. Maps of the attenuation quality factor Q for (a) shear-wave attenuation in the crust (crustal Qs), (b) shear-wave attenuation in the mantle (mantle Qs), (c) compressional-wave attenuation in the crust (crustal Qp), and (d) compressional-wave attenuation in the mantle (mantle Qp). Dark lines indicate plate boundaries from Bird (2003).

there are good reasons to keep the Qs and Qp designations. First, the crustal Q models contribute to the crustal legs of *Pn* and *Sn* phases, and these contributions can be significant for short paths near the *Pn*-*Pg* crossover distance. Second, while a simple two-layer earth model is demonstrated here, the method can be extended by adding additional layers (say sediments, or upper and lower crustal layers). Thus, a layer-based nomenclature is both more correct and more general than a phase-based nomenclature such as Q_{Lg} and Q_{Pg}.

The crustal Qs map (Fig. 4a) looks similar to the results we found in Pasyanos *et al.* (2009). While this map is primarily derived from the amplitudes of *Lg* phases, it also includes the crustal legs of *Sn*. The addition of data to the north enhances and better isolates the lateral variation of the low-attenuation region (Kazakh platform) suggested in the first study. More amplitude measurements in the subcontinent do not extend the region of high Q further southeast, at least not with the current sparse coverage. The addition of crustal legs from the *Sn* phase does not seem to have altered the pattern of attenuation anomalies significantly from the previous study.

The attenuation is high (low Q) in the Turkish–Iranian plateau and the Zagros Mountains, with the highest attenuation found in eastern Turkey ($Q = 100$–200). We find moderate attenuation (average Q) along the Red Sea and Arabian platform, and low attenuation (high Q) in the Arabian shield, Tajik Basin, and Indian shield. Overall, the mean Qs in the crust is 307 and the range (determined by the mean plus and minus two standard deviations in log space) is 174–541.

Figure 4b shows upper mantle Qs, which is derived exclusively from *Sn* amplitudes. The mean and range in this case is 452 and 169–1210. It is important to keep in mind that phases such as *Sn* and *Pn* sample the upper mantle lid (at least where it exists) and are not necessarily representative of the rest of the upper mantle. We find high attenuation along the Red Sea, Arabian shield, the Zagros Mountains, and the Turkish–Iranian plateau. The attenuation appears particularly high in eastern Turkey. We find low attenuation in the eastern Arabian platform, Tajik Basin, northwest India, and Pakistan. Outside of the rift zones, there tends to be low attenuation in regions of oceanic crust, including the eastern Mediterranean, south Caspian, and, to a lesser extent, the Black Sea. If we compare our Qs map to the *Sn* efficiency maps of Gök *et al.* (2003) and Al–Damegh *et al.* (2004), we see a remarkable similarity.

Crustal Qp is shown in Figure 4c. This map is mainly derived from the amplitudes of *Pg* phases, but also includes the crustal legs of *Pn*. We find a mean Q of 338 with a range of 206–554. The attenuation is high along the Red Sea, the Turkish plateau, and much of the Iranian plateau. Like crustal Qs, we still see low attenuation in the Tajik Basin, Indian shield, and northern Arabian platform, but it is not as strong in the Indian shield and Arabian platform/shield. The attenuation in the Makran differs from the attenuation in the Iranian plateau to the north. Unlike mantle Qs, we find a wide swath of high attenuation extending from the Red Sea east into the Arabian shield.

The last panel (Fig. 4d) shows upper mantle Qp, which is derived exclusively from *Pn* amplitudes. The mean and range of mantle Qp are 1098 and 193–6228. The values of this parameter are significantly higher and have a wider range than crustal Qp (~350). Like *Sn*, *Pn* samples the upper mantle lid and, therefore, is sensitive to attenuation at these depths. We see high attenuation running from a ridge along the Red Sea and Dead Sea rift east into western Arabia. We also find high attenuation under the Turkish plateau and, to a lesser extent, the Iranian plateau. With better coverage of the area from *Pn*, we can start to see differences between the attenuation of Phanerozoic western Europe and the Precambrian eastern European platform along the Trans-European suture zone. Attenuation is low in eastern Arabia, the eastern Mediterranean, and the southern Caspian. The patterns of anomalies resemble those of mantle Qs, but there appear to be some large differences between mantle Qp and Qs in northern Arabia. Values of Q compare favorably to the results of Morozov *et al.* (1998), who find $Qp \sim 1500$ at shallow upper mantle depth under the Russian platform.

We summarize the average and range of attenuation in our study area in Table 3. If we compare our results to the teleseismic body-wave study of Der *et al.* (1986), they find in the EURS Q model of the Eurasian shield at 1.0 Hz 365–445 for Qs and 800–1000 for Qp in the crust, and 200–263 for Qs and 450–800 for Qp in the mantle lid and low velocity zone. In general our Qs is within their range or lower than these results, but that is not unexpected when comparing the tectonic Tethys Belt with a lower attenuation shield region. However, we find a lower Qp in the crust and higher Qp in the mantle than the EURS model with the assumed $Qp = (9/4)Qs$ relation. Differences in the upper mantle could also be due, in part, to the depth sensitivities of the two methods. Our method is primarily sensitive to the lid, while t^* studies are more sensitive to bulk attenuation. Also, on any direct comparisons of Q, the large tradeoff between the values of Q and the geometrical spreading must be considered.

Using the inversion results, we can take a cross-section through any arbitrary slice of our crust and upper mantle attenuation model. Perhaps one of the most interesting profiles is one spanning from the African platform, across the Arabian Peninsula and the Zagros Mountains, into the Iranian plateau. This cross-section (shown in Fig. 5) highlights one of the key observations of this study: in some regions there are large differences in the relative attenuation of the crust and mantle. What we find is that, while the high crustal attenuation in the Red Sea is fairly spatially limited, it spreads to the northeast under the Arabian shield in the mantle. This is consistent with low *Pn* and *Sn* velocities found under this region (e.g., Ritzwoller *et al.*, 2002). Furthermore, we find very high Q under the Arabian platform, where the lithosphere is thick (Hansen *et al.*, 2007). To the southwest, the moderate attenuation of the African platform is expected given the thinner lithospheric thickness of the Saharan metacraton (Pasyanos and Nyblade, 2007). To the northeast, the high Q is terminated by the Zagros Mountains in the crust and by the Iranian plateau in the mantle.

In addition to lateral attenuation, we also invert for site and source terms. Using equations (2) and (3), we can interpret the source terms as changes to the M_o. It appears that

Table 3
Mean and 2 Standard Deviation Range of Q from This Article

	P wave	*S* wave
Crust	338 (206–554)	307 (174–541)
Upper mantle	1098 (193–6228)	452 (169–1210)

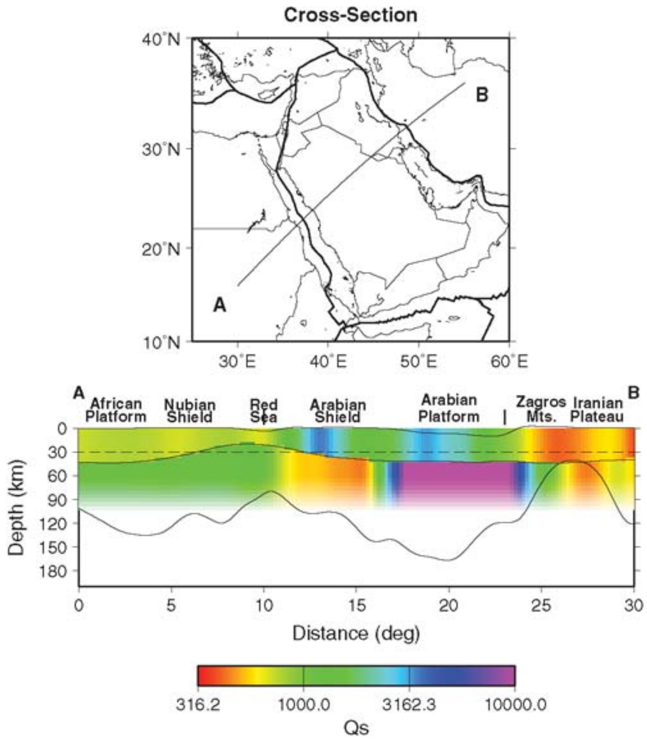

Figure 5. Cross-section from Africa (A) extending northwest across the Arabian Peninsula into Iran (B). The cross-section shows the shear-wave attenuation factor in the crust and mantle along the profile. Solid lines in the profile represent, with increasing depth, basement depth (from Laske and Masters, 1997), Moho depth (modified from Pasyanos *et al.*, 2004), and lithospheric–asthenospheric boundary (LAB) depth (Pasyanos, 2009). Dashed line is the 30 km depth.

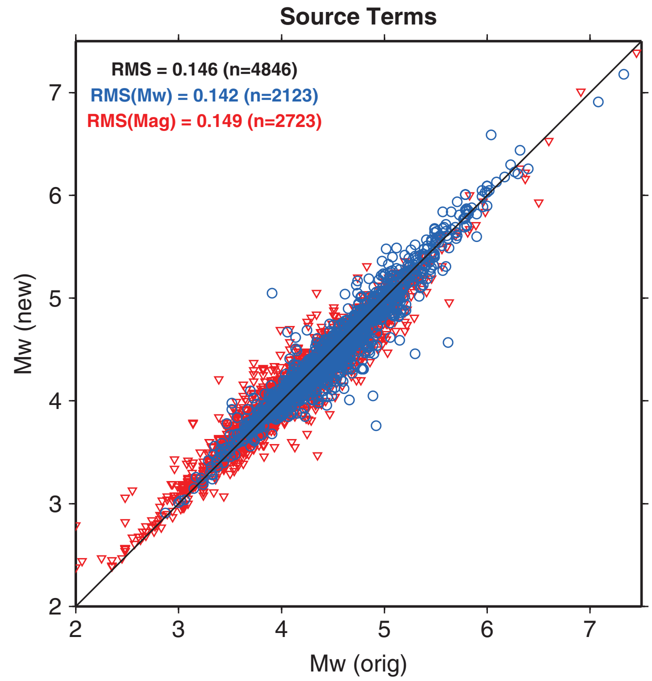

Figure 6. Plot showing a comparison of the inverted moment magnitudes to original moment magnitude estimates. Symbols indicate either moment estimates (blue circles) or converted magnitude estimates (red inverted triangles).

moment terms are somewhat more constrained than in our previous study. In Pasyanos *et al.* (2009), we included events recorded by a single station for a single phase; hence, there was some nonuniqueness in how much of the amplitude was affected by site term changes or attenuation changes along the path. Constraints in that case came from other paths traversing the same region. With several phases recording an event having appropriate source terms for a given moment, there is less ambiguity in the distribution of amplitude effects. Figure 6 shows a comparison of the moment derived from the inverted source term compared with the input moment estimates. The root mean square (rms) difference between the two is about 0.146 magnitude units (m.u.), which is significantly less than the 0.209 m.u. rms that we found in Pasyanos *et al.* (2009). Like that study, we find that true moments vary less in the inversion than moments derived from other magnitude estimates.

We display the *S*-wave and *P*-wave site terms on a map (Fig. 7a and 7b, respectively). The standard deviation of site terms is 0.36 in log-amplitude for *S* and 0.28 for *P*. Several things are observed. First, site terms tend to be higher in shields and platforms and lower in tectonic regions. Beyond this general trend, however, there is variability over small scales. It appears that *P*-wave and *S*-wave site terms are somewhat correlated. When we directly compare the *P*-wave site terms to the *S*-wave site terms (Fig. 7c), we find that they show some similarities, but not overwhelmingly so. The correlation parameter between the two is 0.41, indicating weak correlation. This justifies the use of separate site terms for *P* and *S*.

Returning to attenuation, the last parameters that we compare are the ratios of Qp/Qs for the crust and upper mantle (Fig. 8). Only model points having more than a threshold number of hits (3) are plotted. The correlations here are surprisingly weak given the similarity of some of the maps in Figure 4. It does not appear that relations such as $Qp = (9/4)Qs$ well characterize the relation between the observed *P*-wave and *S*-wave attenuation. For the crust, neither Qp nor Qs is systematically larger, although it does appear that Qp is usually greater than Qs in the mantle. When scattering dominates over intrinsic friction, the compressional and shear-wave quality factors are approximately equal (Richards and Menke, 1983). It appears then that scattering Q might play a larger role in crustal attenuation, particularly in regions such as shields where the intrinsic attenuation is low.

Conclusions

Making use of a new attenuation formulation that explicitly defines the source expression in terms of M_o, we use the amplitudes of regional phases *Pn*, *Pg*, *Sn*, and *Lg* to determine the seismic attenuation of the lithosphere across our

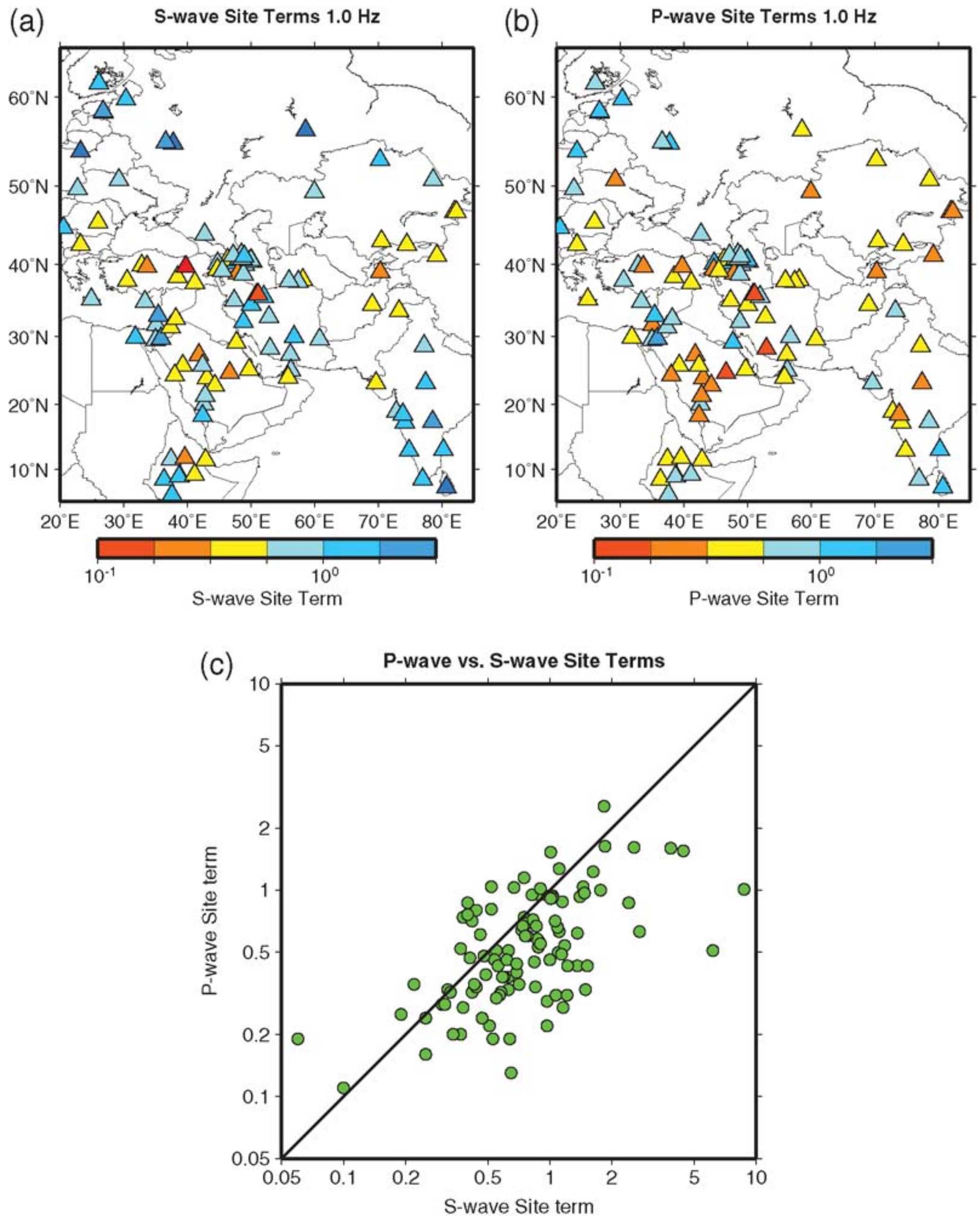

Figure 7. Site term maps showing (a) the *S*-wave source term, and (b) the *P*-wave source term. (c) A comparison of the *P*-wave and *S*-wave site terms.

study area. By taking advantage of the differing sampling of the earth for the four phases, we can isolate the *P*-wave and *S*-wave attenuation of the crust and upper mantle, while consistently accounting for source and site effects.

What we find are patterns in the attenuation maps that relate to the overall tectonic activity of the region. What is most clearly indicated is that thermal altering of the crust and upper mantle increases seismic attenuation. For example, ridges, orogenic zones, and high plateaus being thermally supported have high crustal attenuation. Nearby, undisturbed shields and platforms have low crustal attenuation. In the mantle, we find that regions with well-developed mantle lids have low attenuation, while regions with recent and ongoing tectonic activity have high mantle attenuation. While undisturbed shields and platforms have high Q in both the crust and the mantle, regions with more recent mantle activity see significant differences between them.

On average, we find that values of mantle Q are higher than crustal Q for both Qp and Qs. However, large variations in this parameter from region to region make this far from a universal feature. Whereas in the crust both Qp and Qs generally range from 200 to 500, in the mantle Qs has about the same range, but Qp ranges from 200 to 5000. Surprisingly, we also find that values of *P*-wave attenuation and *S*-wave

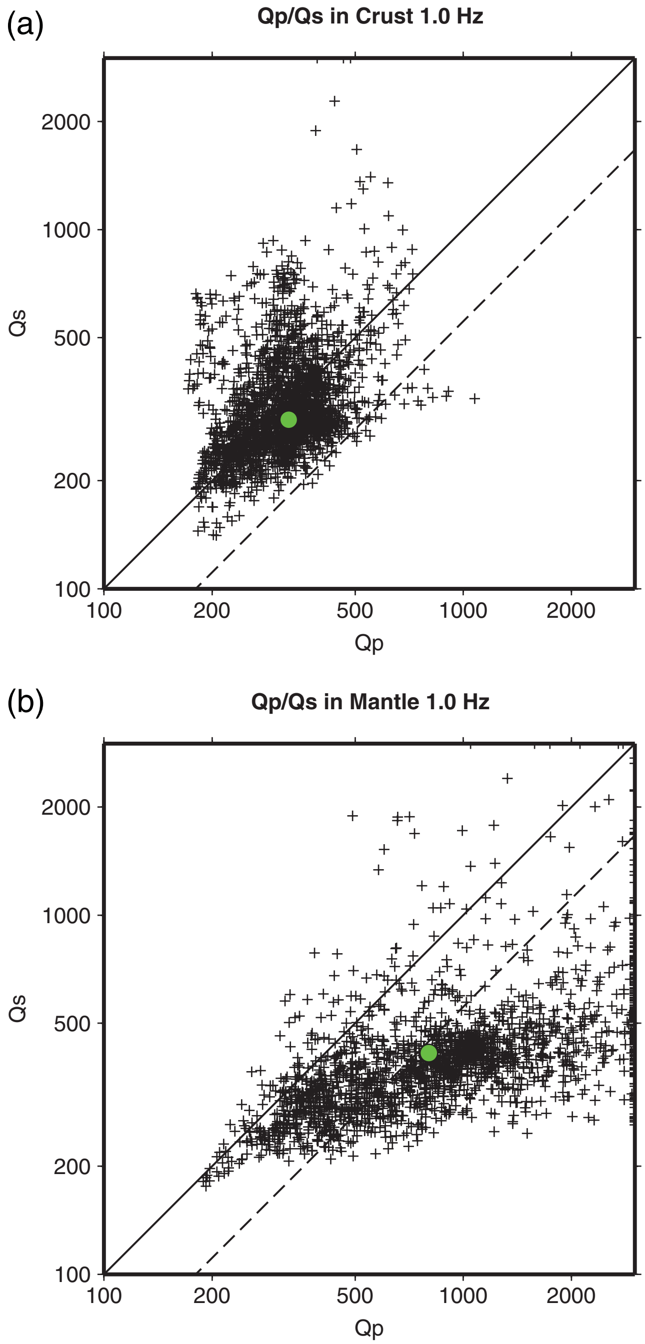

Figure 8. A comparison of Qp and Qs for (a) the crust and (b) the mantle. The solid line shows $Qp = Qs$, while the dashed line indicates $Qp = (9/4)Qs$. Initial values used in the inversion are shown by the green circles.

attenuation are somewhat comparable, particularly in the crust, which may indicate that scattering Q (which is probably on the same order for P and S) is a larger component of total Q than intrinsic Q, which we would expect to be higher for compressional waves.

In order to demonstrate the technique, we have made a number of approximations. Future work could focus on making more exact path calculations. For example, we could add more crustal (and upper mantle) layers and employ a better ray tracer. Similarly, we could put in variable crustal velocity and crustal thickness. We can implement these improvements as regional amplitude data increase enough to justify them.

Data and Resources

Most of the seismic data used in this study can be obtained from the Incorporated Research Institutes in Seismology Data Management Center at www.iris.edu, the U.S. National Data Center at www.tt.aftac.gov, GEOSCOPE at geoscope.ipgp.jussieu.fr, IIEES at www.iiees.ac.ir, GEOFON at geofon.gfz-potsdam.de, and MEDNET at http://mednet.rm.ingv.it. Other data were obtained directly from networks in Azerbaijan, Georgia, Israel, Jordan, Kazakhstan, Kuwait, Oman, Saudi Arabia, Turkey, and United Arab Emirates. Plots were made using the Generic Mapping Tools version 4.2.0 (Wessel and Smith, 1998; www.soest.hawaii.edu/gmt).

Acknowledgments

We thank Doug Dodge and Mike Ganzberger for the regional body-wave amplitude processor tool; Artie Rodgers and Rengin Gök for their efforts providing seismic data; Stan Ruppert and Terri Hauk for maintaining our seismic database; and Flori Ryall for her regional picks. We thank editor Robert Nowack, reviewer Xiaoning (David) Yang, and an anonymous reviewer for their comments. This work was performed under the auspices of the U.S. Department of Energy by Lawrence Livermore National Laboratory under Contract DE-AC52-07NA27344. This is LLNL contribution LLNL-JRNL-410961.

References

Al–Damegh, K., E. Sandvol, A. Al–Lazki, and M. Barazangi (2004). Regional seismic wave propagation (*Lg* and *Sn*) and *Pn* attenuation in the Arabian Plate and surrounding regions, *Geophys. J. Int.* **157,** 775–795, doi 10.1111/j.1365-246X.2004.02246.x.

Anderson, D. L., and R. S. Hart (1978). *Q* of the earth, *J. Geophys. Res.* **83,** 5869–5882.

Bird, P. (2003). An updated digital model of plate boundaries, *G-cubed* **4,** 1027, doi 10.1029/2001GC000252.

Boore, D. M., and J. Boatwright (1984). Average body-wave radiation coefficients, *Bull. Seismol. Soc. Am.* **74,** 1615–1621.

Chavez, D., and K. F. Priestley (1986). Measurement of frequency dependent *Lg* attenuation in the Great Basin, *Geophys. Res. Lett.* **13,** 551–554.

Der, Z. A., A. C. Lees, and V. F. Cormier (1986). Frequency dependence of *Q* in the mantle underlying the shield areas of Eurasia, Part III: The *Q* model, *Geophys. J. R. Astr. Soc.* **87,** 1103–1112.

Gök, R., E. Sandvol, N. Turkelli, D. Seber, and M. Barazangi (2003). *Sn* attenuation in the Anatolian and Iranian plateau and surrounding regions, *Geophys. Res. Lett.* **30,** 8042, doi 10.1029/2003GL018020.

Gök, R., N. Turkelli, E. Sandvol, D. Seber, and M. Barazangi (2000). Regional wave propagation in Turkey and surrounding regions, *Geophys. Res. Lett.* **27,** 429–432.

Hansen, S. E., A. J. Rodgers, S. Y. Schwartz, and A. M. S. Al–Amri (2007). Imaging ruptured lithosphere beneath the Red Sea and Arabian Peninsula, *Earth. Planet. Sci. Lett.* **259,** 256–265, doi 10.1016/j.epsl.2007.04.035.

Laske, G., and G. Masters (1997). A global digital map of sediment thickness, *Eos Trans. AGU* **78,** F483.

Levshin, A. L., M. P. Barmin, X. Yang, and M. H. Ritzwoller (2008). Toward a Rayleigh wave attenuation model for Asia and surrounding regions, in *Proc. of the 30th Monitoring Research Review of Ground-Based Nuclear Explosion Monitoring Technologies*, Portsmouth, Virginia, September 23–25, 2008, 10 pp.

McCormack, D. A., K. F. Priestley, and H. J. Patton (1994). Distance effects on regional discriminants along a seismic profile in Northwest Nevada; NPE and nuclear results, in *Proc. of the Symposium on the Non-Proliferation Experiment*, M. Denny (Editors), Lawrence Livermore National Laboratory, CONF-9404100, p. 6-254–6-271.

McNamara, D., and W. Walter (2001). Mapping crustal heterogeneity using *Lg* propagation efficiency throughout the Middle East, Mediterranean, southern Europe and northern Africa, *Pure Appl. Geophys.* **158,** 1165–1188.

Mellors, R., F. Vernon, V. Camp, A. M. Al–Amri, and A. Gharib (1999). Regional waveform propagation in the Saudi Arabian Peninsula and evidence for a hot upper mantle under western Arabia, *J. Geophys. Res.* **104,** 20,221–20,235.

Mitchell, B. J., Y. Pan, J. Xie, and L. Cong (1997). *Lg* coda *Q* variation across Eurasia and its relation to crustal evolution, *J. Geophys. Res.* **102,** 22,767–22,779.

Morozov, I. B., E. A. Morozova, S. B. Smithson, and L. N. Solodilov (1998). 2-D image of seismic attenuation beneath the Deep Seismic Sounding profile "Quartz", Russia, *Pure Appl. Geophys.* **153,** 311–343.

Olsen, K. B., S. M. Day, and C. R. Bradley (2003). Estimation of *Q* for long-period (2 sec) waves in the Los Angeles Basin, *Bull. Seismol. Soc. Am.* **93,** 627–638.

Pasyanos, M. E. (2009). Lithospheric thickness modeled from long period surface wave dispersion, *Tectonophysics* doi 10.1016/j.tecto.2009.02.023.

Pasyanos, M. E., and A. A. Nyblade (2007). A top to bottom lithospheric study of Africa and Arabia, *Tectonophysics* **444,** 27–44, doi 10.1016/j.tecto.2007.07.008.

Pasyanos, M. E., E. M. Matzel, W. R. Walter, and A. J. Rodgers (2009). Broad-band *Lg* attenuation modeling in the Middle East, *Geophys. J. Int.* **177,** 1166–1176, doi 10.1111/j.1365-246X.2009.04128.x

Pasyanos, M. E., W. R. Walter, M. P Flanagan, P. Goldstein, and J. Bhattacharyya (2004). Building and testing an *a priori* geophysical model for Western Eurasia and North Africa, *Pure Appl. Geophys.* **161,** 235–281.

Richards, P. G., and W. Menke (1983). The apparent attenuation of a scattering medium, *Bull. Seismol. Soc. Am.* **73,** 1005–1021.

Ritzwoller, M. H., M. P. Barmin, A. Villaseñor, A. L. Levshin, and E. R. Engdahl (2002). *Pn* and *Sn* tomography across Eurasia to improve regional seismic event locations, *Tectonophysics* **358,** 39–55.

Sandvol, E., K. Al–Damegh, A. Calvert, D. Seber, M. Barazangi, R. Mohamed, R. Gok, N. Turkelli, and C. Gurbuz (2001). Tomographic imaging of *Lg* and *Sn* propagation in the Middle East, *Pure Appl. Geophys.* **158,** 1121–1163.

Sereno, T. J., S. R. Bratt, and T. C. Bache (1988). Simultaneous inversion of regional wave spectra for attenuation and seismic moment in Scandinavia, *J. Geophys. Res.* **93,** 2019–2036.

Storchak, D. A., J. Schweitzer, and P. Borman (2003). The IASPEI standard seismic phase list, *Seism. Res. Lett.* **74,** 761–771.

Street, R. L., R. Herrmann, and O. Nuttli (1975). Spectral characteristics of the *Lg* wave generated by central United States earthquakes, *Geophys. J. R. Astr. Soc.* **41,** 51–63.

Taylor, S. R., A. A. Velasco, H. E. Hartse, W. S. Phillips, W. R. Walter, and A. J. Rodgers (2002). Amplitude corrections for regional seismic discriminants, *Pure Appl. Geophys.* **159,** 623–650.

Walter, W. R., and S. R. Taylor (2001). A revised magnitude and distance amplitude correction (MDAC2) procedure for regional seismic discriminants: theory and testing at NTS, Lawrence Livermore National Laboratory, UCRL-ID-146882 www.llnl.gov/tid/lof/documents/pdf/240563.pdf.

Wessel, P., and W. H. F. Smith (1998). New, improved version of Generic Mapping Tools released, *Eos Trans. AGU* **79,** 579.

Yang, X. (2002). A numerical investigation of *Lg* geometrical spreading, *Bull. Seismol. Soc. Am.* **92,** 3067–3079.

Yang, X., T. Lay, X.–B. Xie, and M. S. Thorne (2007). Geometric spreading of *Pn* and *Sn* in a spherical earth model, *Bull. Seismol. Soc. Am.* **97,** 2053–2065, doi 10.1785/0120070031.

Zhang, T. R., and T. Lay (1995). Why the *Lg* phase does not traverse oceanic crust, *Bull. Seismol. Soc. Am.* **85,** 1665–1678.

Zhang, J., T. Lay, J. Zaslow, and W. R. Walter (2002). Source effects on regional seismic discriminant measurements, *Bull. Seismol. Soc. Am.* **92,** 2926–2945.

Zor, E., E. Sandvol, J. Xie, N. Türkelli, B. Mitchell, A. H. Gasanov, and G. Yetirmishli (2007). Crustal attenuation within the Turkish Plateau and surrounding regions, *Bull. Seismol. Soc. Am.* **97,** 151–161.

Lawrence Livermore National Laboratory
7000 East Avenue L-046
P.O. Box 808 Livermore, California 94551

Manuscript received 2 March 2009